Journal of Hazardous Materials 443 (2023) 130298

Contents lists available at ScienceDirect

Journal of Hazardous Materials

journal homepage: www.elsevier.com/locate/jhazmat

Research Paper

Integrating FTIR 2D correlation analyses, regular and omics analyses studies on the interaction and algal toxicity mechanisms between graphene oxide and cadmium

Kangying Wu, Yuhao Li, Qixing Zhou *, Xiangang Hu, Shaohu Ouyang *

Key Laboratory of Pollution Processes and Environmental Criteria (Ministry of Education)/Tianjin Key Laboratory of Environmental Remediation and Pollution Control, College of Environmental Science and Engineering, Nankai University, Tianjin 300350, China

HIGHLIGHTS

- Binding mechanisms of Cd^{2+} onto GO at the molecular level in aqueous phase.
- Cd^{2+} inhibited the colloidal stability of GO in BG-11 medium.
- Co-exposure with GO amplified the toxicity of Cd^{2+} to *Chlorella vulgaris*.
- Joint omics reveal GO nanosheets augment the phytotoxicity of Cadmium.

GRAPHICAL ABSTRACT

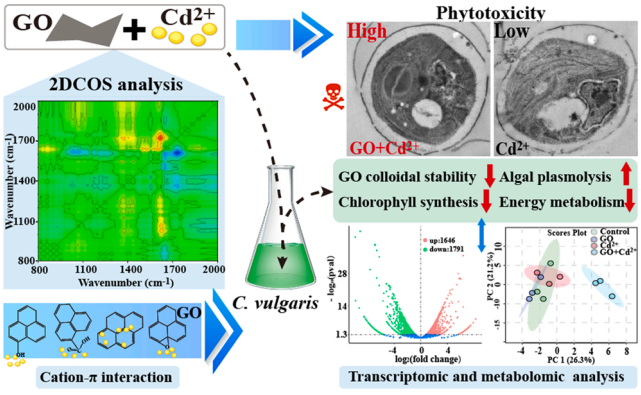

ARTICLE INFO

Editor: Lingxin Chen

Keywords:
Graphene-based nanomaterials
Inorganic pollutant
Environmental fate
Toxicity
Molecular mechanism

ABSTRACT

Graphene oxide (GO, a popular 2D graphene-based nanomaterial) has developed quickly and has received considerable attention for its applications in environmental protection and pollutant removal. However, significant knowledge gaps still exist about the interaction characteristic and joint toxicity mechanism of GO and cadmium (Cd) on aquatic organisms. In this study, GO showed a high adsorption capacity (120. 6 mg/g) and strong adsorption affinity (K_L = 0.85 L/mg) for Cd^{2+}. Integrating multiple analytical methods (e.g., electron microscopy, Raman spectra, and 2D correlation spectroscopy) revealed that Cd^{2+} is uniformly adsorbed on the GO surface and edge mainly through cation-π interactions. The combined ecological effects of GO and Cd^{2+} on *Chlorella vulgaris* were observed. Cd^{2+} induced more severe growth inhibition, photosynthesis toxicity, ultrastructure damage and plasmolysis than GO. Interestingly, we found that GO nanosheets could augment the algal toxicity of Cd^{2+} (e.g., chlorophyll b, mitochondrial membrane damage, and uptake). Transcriptomics and metabolomics further explained the underlying mechanism. The results indicated that the regulation of PSI-, PSII-, and metal transport-related genes (e.g., ABCG37 and ZIP4) and the inhibition of metabolic pathways (e.g., amino acid, fatty acid, and carbohydrate metabolism) were responsible for the persistent phytotoxicity. The

* Corresponding authors.
E-mail addresses: Zhouqx523@126.com, zhouqx@nankai.edu.cn (Q. Zhou), ouyangshaohu@nankai.edu.cn (S. Ouyang).

https://doi.org/10.1016/j.jhazmat.2022.130298
Received 26 July 2022; Received in revised form 14 October 2022; Accepted 30 October 2022
Available online 1 November 2022

present work provides mechanistic insights into the roles of coexisting inorganic pollutants on the environmental fate and risk of GO in aquatic ecosystems.

1. Introduction

In recent years, graphene-based nanomaterials (GBNs) have received increasing attention for their potential application in various areas, such as electronics (Zhu et al., 2021), biomedicines (Ebrahimi et al., 2022; Heerema and Dekker, 2016), biosensors (Ebrahimi et al., 2022; Hashmi et al., 2022), energy-related systems (Zhu et al., 2021), and water treatment (Perreault et al., 2015), due to its excellent antiviral, electrical, morphological, optical and thermal properties. GBNs could produce from nearly carbon-containing anything, such as plants, animals and natural and industrial carbonaceous wastes (Akhavan et al., 2014; Ruan et al., 2011). GBNs will likely be released into the aquatic environments at significant levels with their increasing production and usage. Once released, the GBNs will most likely interact with coexisting pollutants (e.g., organic contaminants and toxic heavy metals), which are widely present in aquatic environments (Peng et al., 2020; Q. Sun et al., 2022; B. Sun et al., 2022; Xu et al., 2020). Investigating the combined ecological effect of GBNs and coexisting pollutants is more environmentally meaningful than learning the ecotoxicity of pristine GBNs or coexisting pollutants alone.

Graphene oxide (GO, a popular and representative GBN) could induce aquatic toxicity to bacteria, algae, and fish, due to its excellent colloidal stability and sharp edges (Akhavan and Ghaderi, 2010; Audira et al., 2021; Ouyang et al., 2020). Furthermore, the mechanisms of GO toxicity have been extensively studied, including physical direct interaction damage (Akhavan and Ghaderi, 2010), generation/explosion of nanobubbles (Jannesari et al., 2020), oxidative stress (Liu et al., 2011), interruption in the glycolysis process (Akhavan and Ghaderi, 2012), DNA damage, and chromosomal aberration (Hashemi et al., 2016). Although limited studies have concentrated on the compound ecological effects of carbon-based materials and metals on the biological organisms (Akhavan et al., 2011; Akhavan et al., 2013; Zhao et al., 2020). For example, Akhavan et al. reported that the bactericidal activity of carbon nanotubes was highly improved by loading silver nanoparticles at their opened tips, and reduced graphene oxide nanoribbons with residual Ni catalysts caused severe genotoxicity human mesenchymal stem cells (Akhavan et al., 2011, 2013).

However, the interaction characteristic and the joint toxicity molecular mechanism of GO and toxic heavy metals (e.g., cadmium) on aquatic organisms are lacking. Generally, some advanced characterization techniques, such as X-ray photoelectron spectroscopy (XPS) and electron paramagnetic resonance (EPR), have been widely used to analyze the interfacial interaction between organic functional groups and heavy metals (Ouyang et al., 2020; Yao et al., 2020). Compared with above advanced characterization techniques, Fourier transform infrared spectra (FTIR) combined with 2D correlation spectroscopy (2DCOS) can resolve overlapped peaks by extending spectra along the second dimension and provide information about the relative directions and sequential orders of structural variations (Chen et al., 2019). Algae, as pivotal primary producers in aquatic environments, are commonly used as model organisms to test the toxic effects of various toxicants (e.g., heavy metals, organic pollutants, and nanoparticles) in aquatic environments (Zeng et al., 2022; Zhao et al., 2020). Herein, we selected *Chlorella vulgaris (C. vulgaris)* as an experimental biological model to explore the combined ecological effects and underlying molecular mechanisms of GO and Cd^{2+}.

In this study, we firstly explored the adsorption of Cd^{2+} onto GO and intensively characterized the interactions between GO and Cd^{2+} using Fourier transform infrared spectra (FTIR) 2D correlation spectroscopy (2DCOS). Before algal toxicity, we observed the effect of Cd^{2+} on the colloidal stability of GO in an algal culture medium. Subsequently, we comprehensively and systematically analyzed the biological response to *C. vulgaris* under the co-exposure of GO and Cd^{2+}, such as growth inhibition, photosynthesis, oxidative stress, Cd uptake, and ultrastructure damage. Finally, "Omics" (transcriptomic and metabolomic analyses) were used to reveal the response pathways and specific molecular mechanisms for compound phytotoxicity. Our findings provide new perspectives on the environmental implications and the management of combined pollution based on GBNs in aquatic ecosystems.

2. Materials and methods

2.1. Preparation and characterization of graphene oxide nanosheets

GO (production number, XF002–1) was purchased from Nanjing XFNANO Materials Tech Co., Ltd., China. The details for the preparation methods and characterization for the GO and GO-Cd conjugates suspensions were presented in Supporting Information (SI) Text S1.

2.2. Adsorption experiments

The adsorption behavior of Cd^{2+} was quantitatively explored at 25 °C and pH 7.0 by traditional batch experiments. In detail, GO (50 mg/L), the various concentrations of Cd^{2+} (0 −40 mg/L), and equal volumes of GO and Cd^{2+} suspensions were mixed in 15 mL vials and then were placed on a rotator with stirring at 160 rpm/min for 12 h. Then centrifugation was performed for solid-liquid separation (10000g, 10 min). 0.45 μm microporous membrane was used for GO (diameter, 0.5 −5 μm) filtration to remove the shadow from the measurement of the free Cd^{2+} in the supernatant via a PerkinElmer Analyst 700 (PE700, USA) atomic absorption spectrometer. The adsorption isotherms of Cd^{2+} on GO were investigated by Langmuir and Freundlich's models. For details, see SI Text S2. Subsequently, the resultant precipitates of GO-Cd conjugates were washed with Mill-Q water to remove the unbound Cd^{2+}. The GO-Cd conjugates were then freeze-dried for subsequent analysis by Fourier infrared spectroscopy (FTIR).

2.3. FTIR measurements and 2DCOS analysis

The freeze-dried GO nanosheets with different Cd^{2+} concentrations were ground homogeneously. Afterward, 0.1 mg of the GO-Cd conjugates (0.1 mg) were lyophilized, mixed with KBr (100 mg), and pressed under infrared lamp irradiation to eliminate the effect of moisture. The FTIR absorption spectra were measured with an infrared spectrometer (Bruker Tensor 27, Germany) at 600–2000 cm^{-1} per spectrum with a resolution of 4 cm^{-1} and an average of 32 scans. The spectra were further analyzed with OPUS 5.5 software. To probe the structural changes of GO binding Cd^{2+}, 2DCOS was employed using FTIR spectra with Cd^{2+} concentration as the external variable. The 2DCOS spectra were manufactured using Noda's and Ozaki' s method (Noda, 2004). See SI Text S3 for the relevant details.

2.4. Aggregation kinetics of GO in the presence of Cd^{2+}

The aggregation of GO has critical impactions for its fate and ecotoxicity risk. Thus, before algal toxicity, the effect of Cd^{2+} on GO aggregation in the blue-green culture medium (BG-11, composition see Table S1) was examined at 25 °C and pH 7.0. The effects of various concentrations of Cd^{2+} (0, 0.1, 1.0, 10 mg/L) on alterations in the GO zeta potential and hydrodynamic diameter (D_h) were detected using a Zetasizer Nano ZS (Malvern Instruments, Malvern, UK). See SI Text S4 for details.

2.5. Algal cell cultivation and toxicity experiments

C. vulgaris, purchased from the Institute of Wuhan Hydrobiology, Chinese Academy of Sciences, was cultured with BG-11 medium in an artificial climate incubator (Shanghai Boxun Medical Biological Instrument Incorporated Company, SPX-300I-C, China). Detailed culture parameters were set at 25.0 ± 0.5 °C, light/dark = 16:8 h, and 80% humidity. Currently, the environmental-related concentrations of GO are still unknown (Goodwin et al., 2018). To investigate the nanotoxicity of GO at predicted environmental concentrations (0.01–1 mg/L) (Ouyang et al., 2020), *C. vulgaris* was exposed to 1.0 mg/L of GO. The environmental concentrations of Cd^{2+} could reach the mg/L level in the global river and lake water bodies (Lavoie et al., 2014). Moreover, the 96-h twenty percent effective concentration (96-h EC_{20}) of Cd^{2+} on *C. vulgaris* was determined to be 1.15 ± 0.43 mg/L (Fig. S1) (the details see SI Text S5). Based on the environmental-related concentrations and 96-h EC_{20} of Cd^{2+}, 0.01, 0.1, and 1.0 mg/L of Cd^{2+} were tested on *C. vulgaris*. Thus, to investigate the combined toxicity of GO and Cd^{2+}, *C. vulgaris* was exposed to BG-11 medium (control), GO (1 mg/L), Cd^{2+} (0.01, 0.1, and 1 mg/L), and GO + Cd^{2+} (1 mg/L GO, 0.01–1 mg/L Cd^{2+}) in 250 mL glass flasks for 96 h exposure.

After 96 h exposure, the intensity of algal cells in the control (N_0) and treatment (N_t) groups was counted by an automatic algae counter (Countstar® BioMarine IA1000, ALIT Life Science Co. Limited, China), and growth inhibition (%) = $(N_0 - N_t)/N_0 \times 100$. Moreover, the chlorophyll a and chlorophyll b contents of algal cells were detected by spectrophotometer, see SI Text S6 for details. The mitochondrial membrane potential (MMP), intracellular ROS level, and cell permeability were detected using 5,5′,6, 6′-tetrachloro-1,1′,3,3′-tetraethyl-imidacarbocyanine iodide (JC-1), 2′,7′-dichlorofluorescein-diacetate (DCFH-DA), and fluorescein diacetate (FDA) fluorescence staining methods, respectively (Li et al., 2022). Detailed measurement of the above indicators was provided in SI Text S7-Text S9.

2.6. Electron microscopic observations

Morphological and cellular microscopic characterization of C. *vulgaris* were detected by scanning electron microscopy (SEM) and transmission electron microscopy (TEM), respectively. See SI Text S10 for details about electron microscopic observation.

2.7. Cellular uptake

After 96 h exposure, algal cell samples were collected and repeatedly washed with BG-11 medium and soaked with EthyleneDiamineTetraaceticAcid, followed by centrifugation to obtain the supernatant and algal pellets. The Cd associated with the supernatant and algal pellets represented the cell-wall bound Cd and intracellular Cd contents, respectively (Xie et al., 2020). The Cd content test was detected by inductively coupled plasma–mass spectrometry (ICP–MS, Elandrce, PerkinElmer, America), and related details were available in SI Text S11.

2.8. Algal transcriptomic and metabolomic analysis

After 96 h exposure, algal cell suspension (20 mL) was harvested by centrifugation (15 min, 4000 g, 4 °C; centrifuge 5810 R, Eppendorf) for transcriptomic and metabolomic analysis. The sampling and RNA isolation of algal cells were described in ref. (Zeng et al., 2022), details were also available in SI Text S11. Transcriptomic analysis was tested at Novogene Bioinformatics Technology Co., Ltd., Tianjin, China. RNA-seq transcription libraries were instituted using the Illumina-HiSeq platform, and differentially expressed genes (DEGs) were analyzed with the edgeR software package. Functional enrichment analysis of Gene Ontology (GO) and (Kyoto Encyclopedia of Genes and Genomes) KEGG pathway enrichment analysis of differential gene sets was performed using GOseq (1.10.0) and KOBAS (v2.0.12) software. The details of the transcriptomic analysis were exhibited in SI Text S11.

For metabolite profiling, the algal cell metabolites were extracted by liquid−liquid extraction, centrifuge enrichment, and freeze-drying (details see SI Text S12). Metabolites were manually methoxyaminated and trimethylsilylated (details see SI Text S12), and subsequently analyzed by gas chromatography−mass spectrometry (GC-MS, 6890 N/5973, Agilent, Santa Clara, CA) as previously described (Zhang et al., 2021). Briefly, the samples (1 μL) were injected into an HP-5MS capillary column (19091S-102, Agilent, USA) in split mode (1:2). The carrier gas was helium with a flow rate of 2 mL/min. The inlet temperature was 230 °C. The column temperature program was set to 80 °C for 2 min, then the temperature was increased to 325 °C at a rate of 15 °C/min for 6 min. The spectrometer was operated in electron-impact mode, and the detection voltage was 1850 V. Using full scan mode, the detection range is *m/z* 70–700, and the acquisition rate is 20 scans/s. The metabolites were identified compared to the National Institute of Standards and Technology (NIST 14.0) library. Finally, the metabolic data were analyzed by MetaboAnalyst 5.0 (http://www.metaboanalyst.ca).

2.9. Statistical analysis

All experiments were performed at least in triplicate. The results were displayed as the mean ± standard deviation. One-way analysis of variance (ANOVA) and Tukey's test using IBM SPSS 22.0 software was used for statistical significance analysis. Before ANOVA, the Kolmogorov-Smirnov (KS) test was also used to assess normal distribution. And when p was less than 0.05, it was considered significant.

3. Results and discussion

3.1. Characterization of GO and GO-Cd nanosheets

As shown in Fig. 1A-H, the morphology of GO and GO-Cd nanosheets was visualized by high-angle annular dark field scanning transmission electron microscopy (HAADF-STEM). GO and the GO-Cd hybrid presented a sheet-like morphology with wrinkles and sharp zigzag edges (as the red arrows indicate). The lateral length of GO ($n > 15$) was approximately 0.5 − 4.5 μm, which follows our previous report for GO (Ouyang et al., 2020). Moreover, the energy dispersive spectroscopy corresponding mapping images showed the elemental distribution of carbon (C), oxygen (O), and Cd on the GO nanosheets. Notably, Cd^{2+} was uniformly adsorbed on the GO surface and edge, and the Cd content in GO increased from 0.16 % to 1.98 % (Table S2). The negligible Cd content (0.16 %) in the original GO nanosheets might be attributed to the process of microscopy artifacts (Vanrompay et al., 2021). Thus, the fair distribution and adsorption of Cd^{2+} on the GO surface could be confirmed.

To further reveal additional physicochemical characterization of the GO samples, UV−vis, solid-state electron paramagnetic resonance (EPR), Raman, and X-ray diffraction (XRD) were performed. The UV adsorption peaks of GO and GO-Cd hybrid were detected at about 235 nm (Fig. 1I), which was attributed to π–π * transitions of the C═C bonds (Li et al., 2018). After Cd^{2+} treatment, a hypochromic effect was detected at 235 nm in the GO-Cd hybrid, demonstrating that Cd^{2+} could bind to the surface of GO through π − π stacking interactions (Sivaranjan et al., 2020). Solid-state EPR was a sensitive and specific technique for characterizing the formation of π-conjugated semiquinone-type free radicals on the GO surface (Scott et al., 1998). As shown in Fig. 1J, GO and GO-Cd hybrid nanosheets showed a similar single resonance peak of the semiquinone-type free radical signal. However, after treatment with Cd^{2+}, the *g*-value of semiquinone-type free radicals in GO shifted from 2.0071 to 2.0095, indicating that Cd^{2+} could directly interact with GO's surface plane via cation-π interactions. This result was in accord with a previous report (Chen et al., 2017). Subsequently, Raman spectroscopy was performed to analyze the structure of GO before and after Cd^{2+} treatments, as shown in Fig. 1K. There were significant characteristic D

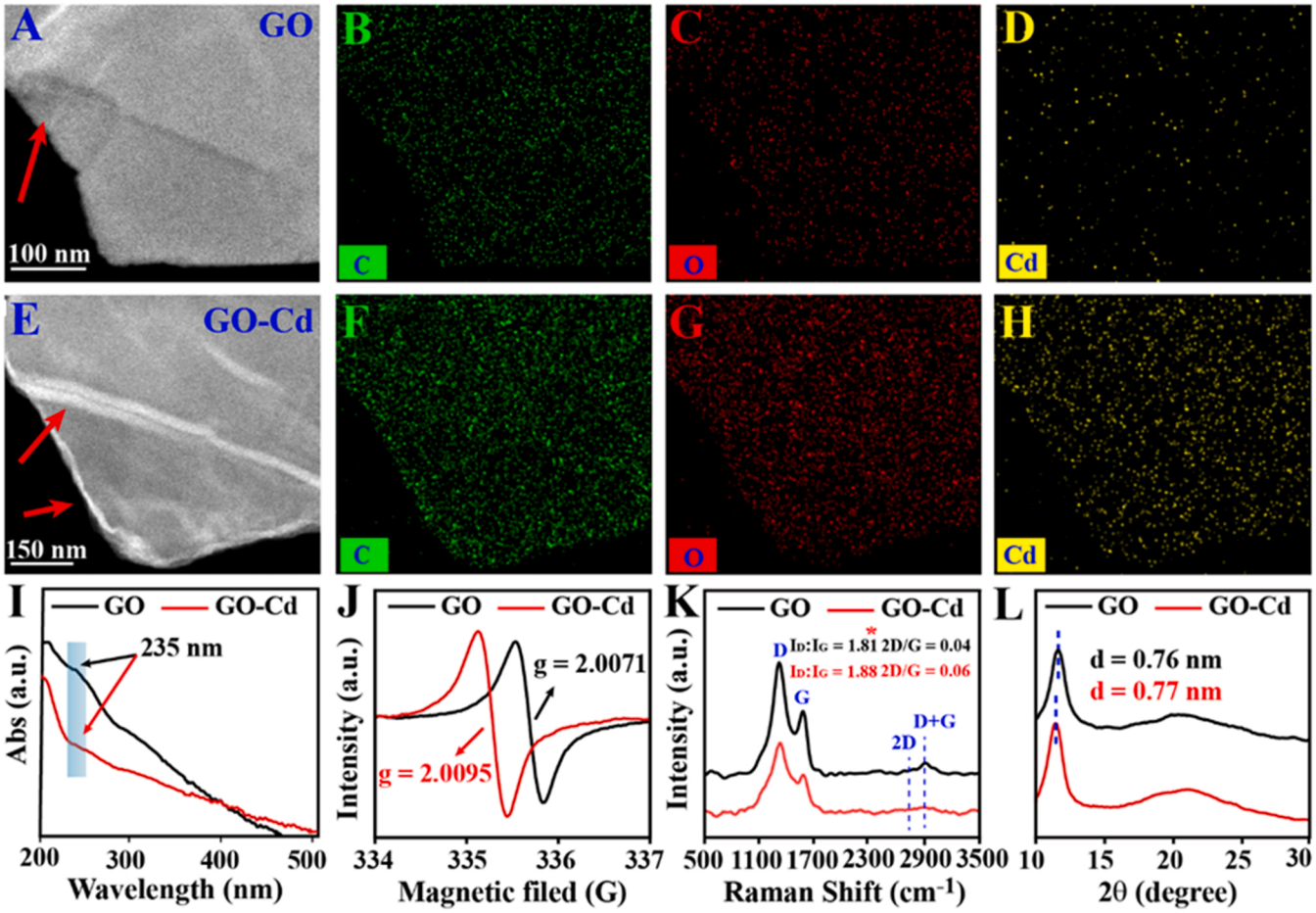

Fig. 1. Characterization of GO and GO-Cd hybrid nanosheets. (A-H) Representative HAADF-STEM ($n > 15$) and the corresponding elemental mappings of GO (A-D) and GO-Cd (E-H). (I) UV–vis spectra ($n = 3$). (J) solid EPR spectra ($n = 3$). (K) Raman spectra ($n = 3$). (L) XRD patterns ($n = 3$).

bands (1310 cm^{-1}), G bands (1580 cm^{-1}), weak 2D bands (2770 cm^{-1}), and D+G bands (2910 cm^{-1}) in the GO and GO-Cd nanosheet samples. Generally, the I_G/I_D ratio provided a measure of carbon structure disorder and had a positive correlation with the amount of sp^2 sites in the GO sample (Akhavan, 2015). The high I_D/I_G ratio of GO (1.81 ± 0.06, $n = 3$) was significantly ($p < 0.05$) different from that in GO-Cd nanosheets (1.88 ± 0.09, $n = 3$), indicating the presence of a decreased amount of sp^2 sites on the surface of GO nanosheets after Cd^{2+} treatment. The result was in accordance with the UV−vis spectra (Fig. 1I). Moreover, the position and intensity of the 2D band were sensitive to the stacking of graphene sheets, and the 2D/G ratio of graphene reflected the layer of graphene sheets (Akhavan, 2015). Here, there was no noticeable difference ($p > 0.05$) in the 2D/G ratio of the GO (0.04 ± 0.01) and GO-Cd nanosheets (0.06 ± 0.01), suggesting that the GO and GO-Cd were typically multi-layer sheets (Hu et al., 2017). The XRD patterns (Fig. 1L) of the GO and GO-Cd hybrid showed strong peaks at $2\theta = 11.62°$ and 11.46°, respectively, identifying highly organized crystal structures. According to Bragg'- s law (Huh, 2014), the D-spacings of GO and GO-Cd were 0.76 ± 0.01 ($n = 3$) and 0.77 ± 0.01 ($n = 3$) nm, respectively, and these values were not significantly different ($p > 0.05$). The XRD results implied that there were no remarkable changes in the crystal structures of GO after Cd^{2+} adsorption (Fig. 1L). This result was also supported by the TEM images (Fig. 1A-H). Taken together with the above characterization data, it was determined that Cd^{2+} was uniformly spread and bonded to the center and edge of GO nanosheets mainly through cation-π interactions. Meanwhile, the adsorption of Cd^{2+} did not induce the remarkable changes in the morphology and conformation of GO nanosheets.

3.2. Adsorption isotherms of Cd^{2+} onto GO and 2DCOS analysis

Adsorption isotherms of Cd^{2+} onto GO were shown in Fig. 2A, and the Langmuir and Freundlich isotherm parameters were presented in Table S3. From the regression coefficient (R^2) (Table S3), the fitting effect of the Langmuir model ($R^2 = 0.999$) was better than the Freundlich model ($R^2 = 0.976$), suggesting that the adsorption sites of Cd^{2+} on GO were homogeneously distributed. This result was corroborated by the HAADF-STEM results (Fig. 1A–H). Quantitatively, the adsorption capacity of Cd^{2+} on GO was 120.56 ± 3.03 mg/g (Table S3), much higher than the 67.49–83.80 mg/g reported in the literature (Tan et al., 2015; Yang et al., 2016). This result might be due to the difference in the types and properties (e.g., size, morphology, surface functional groups, and defects) of GO. Notably, GO showed a strong adsorption affinity (K_L=0.85 ± 0.13 L/mg) for Cd^{2+} (Table S3), suggesting a strong interaction between Cd^{2+} and GO.

To further analyze the interaction between Cd^{2+} and GO, the FTIR spectral characteristics of Cd^{2+}-adsorbed GO are shown in Figure S2. To further analyze the interactions between Cd^{2+} and GO, the FTIR spectral characteristics of Cd^{2+}-adsorbed GO were shown in Fig. S2. There were abundant functional groups containing C═O (1730 cm^{-1}), aromatic C═C bonds (1630 cm^{-1}), carboxy COO (1380 cm^{-1}), epoxide C-O-C (880 cm^{-1}) and C-OH (1060 cm^{-1}) on the surface of GO (Lee and Hur, 2016; Yang et al., 2016). The additional structural changes of GO after adsorption of Cd^{2+} were more clearly illustrated in the different FTIR absorption spectra (Fig. 2B). For example, the peaks corresponding to the asymmetric stretching of aromatic C═C bonds initially barely changed at 0.1–3 mg/L Cd^{2+} and then increased and shifted from 1630

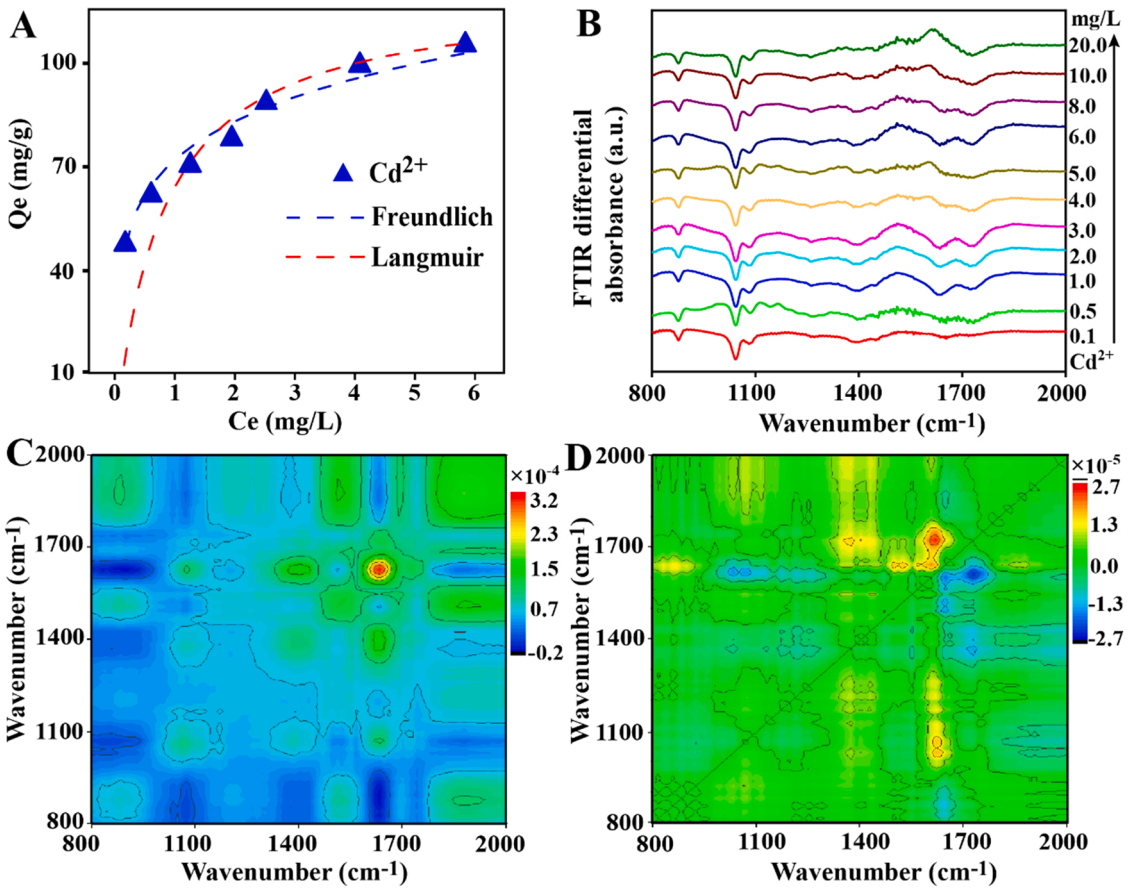

Fig. 2. Adsorption behavior and changes in the FTIR Spectra ($n = 3$) of GO after Cd^{2+} adsorption. (A) Adsorption isotherms of Cd^{2+} onto GO; (B) Differential FTIR absorbance spectra of freeze-dried GO with different Cd^{2+} concentrations (0.1–20 mg/L). (C-D) Synchronous (C) and asynchronous (D) 2DCOS maps generated from FTIR analysis of GO with Cd^{2+} binding in the region of 800 − 2000 cm^{-1}.

to 1620 cm^{-1}at higher concentrations (4–20 mg/L) of Cd^{2+}. This result indicated that there was a cation− π interaction between Cd^{2+} and the aromatic structures of GO, which was also confirmed by the UV−vis (Fig. 1I) and solid EPR (Fig. 1J) results. Additionally, the π − π electron donor−acceptor effect was the main interfacial binding interaction between GO and organic pollutants (e.g., antibiotics and Bisphenol-A) (Yao et al., 2018; Zhang et al., 2016). Even so, the one-dimensional FTIR spectra cannot provide specific information on the exact dynamic binding characteristics of Cd^{2+} to GO.

However, 2DCOS, as a powerful technique, can effectively resolve the above problems by enhancing spectral resolution through the two-dimensional expansion of the spectrum (Chen et al., 2019). Herein, 2DCOS was used to achieve credible monitoring of the conformational alterations of GO induced by Cd^{2+}. The 2D FTIR COS of the interaction between GO and Cd^{2+} at different concentrations were presented in Fig. 2C-2D. Table S4 showed the assignments corresponding to each cross peak. As shown in Fig. 2C, there were five auto peaks in the synchronous map centered at 1630,1525, 1380, 1060, and 880 cm^{-1}. The aromatic C═C bonds of GO could be divided into two peaks (1635 and 1525 cm^{-1}), and the C═C bond peak at 1525 cm^{-1} originated from the reduction of epoxide C-O-C peaks (880 and 1230 cm^{-1}) (Obreja et al., 2013). The peak at 1630 cm^{-1} had the most significant changes, suggesting that the aromatic framework groups of GO played a crucial role in Cd^{2+} capture (Yang et al., 2016). The smallest changes at 1060 and 880 cm^{-1} were related to the stretching of the C−OH of phenol and the C−O−C bending motion, respectively. In the synchronous map, all the cross-peaks were positive, which indicated that all FTIR bands changed in the same direction. Furthermore, seven cross-peaks were observed in the asynchronous map (Fig. 2D), and their detailed assignments of the bands and signs were listed in Table S4. From the Noda rule (Chen et al., 2019), it can be demonstrated that the change sequence of GO backbones structure by Cd^{2+} binding followed the order 1060 > 1380 > 1630 > 880 > 1730 cm^{-1} or C–OH of phenol → carboxyl (COO) → C═C bonds → C−O−C bending motion→ C═O, which suggested that the binding affinity of hydrophilic sites were higher than those of hydrophobic sites. Moreover, coordination is a common and considerable interaction between Cd^{2+} and oxygen-containing groups (like C-O-C, C-OH, -COOH, etc.) of GO (Yao et al., 2020).

3.3. *Cd^{2+} inhibited the colloidal stability of GO in BG-11 medium*

The stability of GO behaviors in environmental or biological media could influence the toxicity of algae (Yang and Wang, 2022; Zhao et al., 2021). Herein, the aggregation profiles of GO in the presence of Cd^{2+} at various concentrations were presented in Fig. S3A. The premier D_h of GO was about 450 nm, then increased to 1720, 1810, 1855, and 1867 nm at 2000 s in the BG-11 medium with 0, 0.1, 1.0, and 10.0 mg/L Cd^{2+}, respectively, indicating that Cd^{2+} slightly promoted the instability of GO. In addition, the initial aggregation rate constant (K_a) could represent the aggregation kinetics of GO, and the result was exhibited in Fig. S3A. The K_a value of GO in the BG-11 medium was 0.697 nm/s, while the K_a of GO increased to 0.698, 0.748, and 0.765 nm/s at Cd^{2+} concentrations of 0.01, 0.1, and 10 mg/L, respectively. As shown in Fig.S3B, the D_h of GO gradually increased from about 500–2500 nm in the BG-11 medium within 96 h, while the D_h of GO with Cd^{2+} was slightly increased. Thus, the GO dispersity in the BG-11 medium was significantly inhibited with the increase of Cd^{2+} concentration from 0.1 to

10 mg/L. This result was consistent with the destabilization capability of other metal cations (e.g., Cr^{3+}, Pb^{2+}, Cu^{2+}, Ca^{2+}, and Mg^{2+}) to GO (Yang et al., 2016). These findings were also supported by the zeta potential data in Fig. S3C and D. The zeta potential of GO in the BG-11 medium decreased with increasing pH (1−7), while those of GO+Cd^{2+} were higher than pure GO at pH values of 4–7 (Fig. S3C). Particularly at pH= 7 in the BG-11 medium, the zeta potential of GO was lower than that of GO with Cd^{2+} within 96 h (Fig. S3D), indicating that Cd^{2+} decreased the electrostatic repulsion of GO in the BG-11 medium, resulting in an increased agglomeration tendency. Cd^{2+} weakened the negative charges and hydrophilicity of the GO surface through oxygen-containing groups coordination and cationic-π interactions (for example, Cd^{2+} crossing the electric double-layer and directly binding to GO) (Yang et al., 2016), which could result in accelerating GO agglomeration. The variations in hydrodynamic and electrokinetic properties clarified that Cd^{2+} slightly inhibited the colloidal stability of GO in the BG-11 medium.

3.4. Combined algal cytotoxicity of GO and cadmium

After 96 h exposure, the growth inhibition of GO, Cd^{2+}, and GO+Cd^{2+} was 9.3 %, 1.5–20.1%, and 12.1–18.6 %, respectively, as shown in Fig. 3 A. The inhibition ratios of GO (1 mg/L) were closed to the reported toxicity of GO toward *C. vulgaris* (Ouyang et al., 2020).

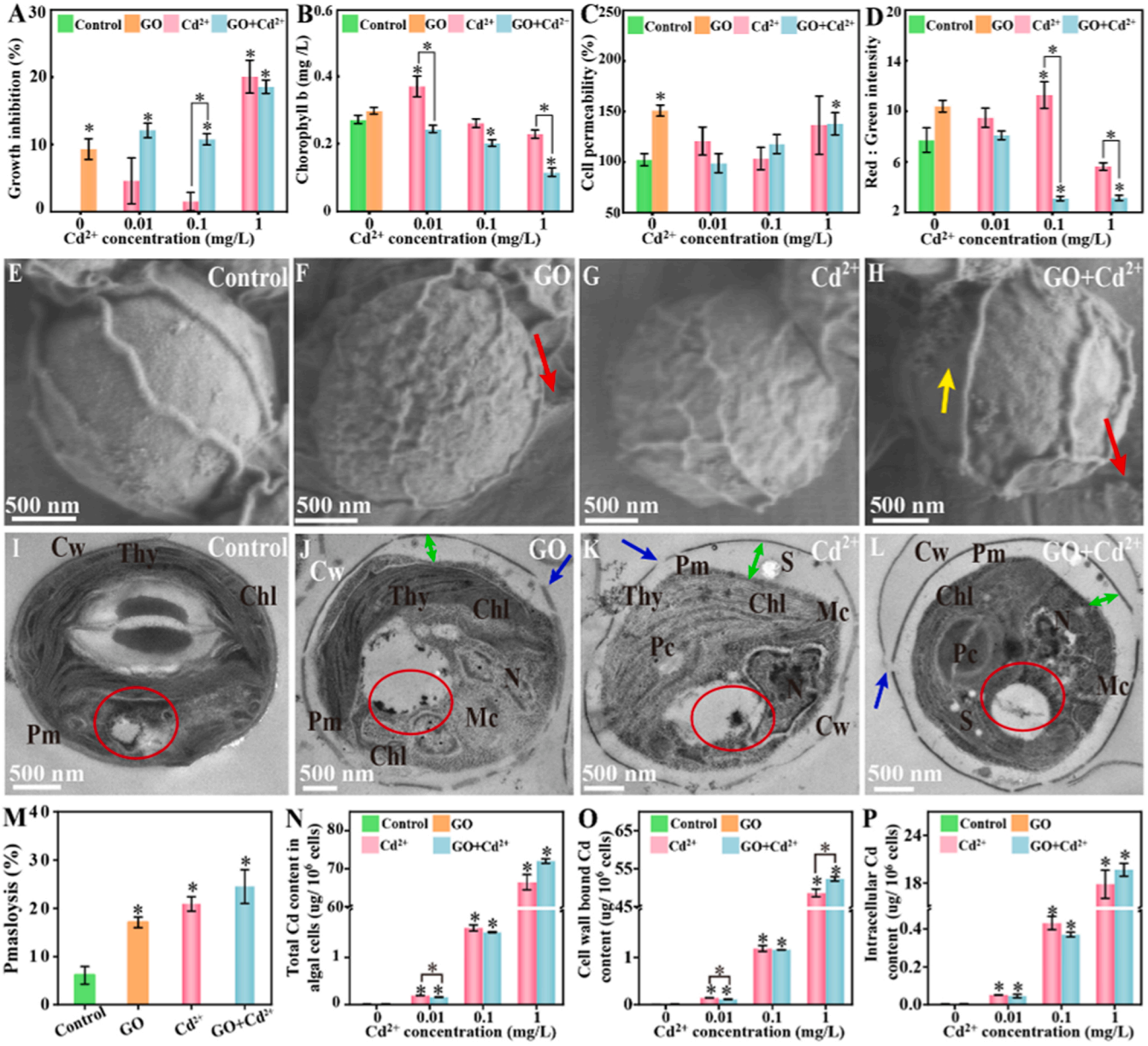

Fig. 3. Toxic effects of GO, Cd^{2+} and GO+Cd^{2+} on *C. vulgaris* at 96 h. (A) Growth inhibition. (B) Chlorophyll b content ($n = 5$). (C) Cell permeability ($n = 5$). (D) Mitochondrial membrane potential (MMP) ($n = 5$). (E-H) Representative SEM images ($n > 15$) of the algae in the absence (E) and presence of GO (F), Cd^{2+} (G) and GO+Cd^{2+} (H). The red and yellow arrows denote adhesion and/or edge contact of GO on algal cellular membranes and secretion adhering to the cell surface, respectively. (I-L), representative TEM images ($n > 15$) of the algae in the absence (I) and presence of GO (J), Cd^{2+} (K) and GO+Cd^{2+} (L), abbreviations: Cw, cell wall; Pm, plasma membrane; S, starch grain; Chl, chloroplast; Pc, pyrenoid center; N, nucleus; Mc, mitochondria. The blue and double green arrows denote cell wall damage and plasmolysis and uptake, respectively, and the red circle denotes the EDS scanning locus (TEM-EDS mapping is shown in Fig. S7). (M) Plasmolysis of algal cells. (N) Content of total Cd in algal cells. (O) Intracellular Cd content. (P) Cell wall-bound Cd content; The black asterisk "* " represents statistical significance at $p < 0.05$.

After exposure to Cd^{2+} treatment groups for 96 h, no significant inhibition was found at 0.01 or 0.1 mg/L, algal growth was significantly ($p < 0.05$) inhibited at 1 mg/L, suggesting that the algal cells were low sensitive to Cd^{2+} (at 0.01–0.1 mg/L) (Le Faucheur et al., 2005). Moreover, the growth inhibition rates in the GO-Cd groups at 1 mg/L Cd^{2+} were 6.5 % and 7.8 % higher than the GO-Cd groups at 0.01 and 0.1 mg/L Cd^{2+}, respectively. Remarkably, the inhibition rate caused by GO at 1 mg/L was significantly ($p < 0.05$) lower than that induced by Cd^{2+} (1 mg/L), indicating that Cd^{2+} induced more potent inhibition of cell division than GO. This result was also supported by previous reports on the toxicities of Cd and GO in mice (Akhavan et al., 2015, 2016). Chlorophyll a and b are the primary photosynthetic pigments in the photosystem and play a crucial role in algal cell growth (Cho et al., 2019). Compared with the control group, there was no significant diversity in chlorophyll a content in exposure groups, except for GO+Cd^{2+} at 1 mg/L (Fig S4). Moreover, the chlorophyll b content was significantly ($p < 0.05$) decreased in 0.1 − 1 mg/L GO+Cd^{2+} exposure groups (Fig. 3B). Interestingly, GO+Cd^{2+} at 1 mg/L presented a more significant ($p < 0.05$) decrease in chlorophyll b content than GO or Cd^{2+} alone at 96 h, indicating that GO+Cd^{2+} induced phototoxicity was higher compared with the control, GO-, or Cd^{2+}-exposed cells, and the corresponding toxicity mechanisms were investigated and discussed in the following section.

Both GO and GO+Cd^{2+} at 1 mg/L induced significant algal cell membrane damage ($p > 0.05$), while other exposure groups had no apparent damage to the membrane. Overall, the addition of Cd^{2+} reduced the destruction of algal cell membranes by GO, which may be related to the surface properties and agglomeration behavior of GO (Gao et al., 2018; Zhao et al., 2014). Furthermore, the Cd^{2+} could also alleviate bacterial cell membrane damage has been reported (Gao et al., 2018). The intracellular homeostasis of the mitochondrial membrane potential (MMP) was also interfered, as shown in Fig. 3D. In comparison with the control group, the red-to-green fluorescence intensity significantly ($p < 0.05$) decreased by 60.8–61.5 % in response to GO+Cd^{2+} at 0.1–1 mg/L exposure. Notably, the red-to-green fluorescence intensity of the GO+Cd^{2+} (at 0.1–1 mg/L) groups was significantly down-regulated compared with that of GO or Cd^{2+} alone, indicating that GO+Cd^{2+} triggered more significant mitochondrial membrane damage than GO and Cd^{2+}. Cellular ROS generation is a common pathway of cytotoxicity (Liu et al., 2011). As shown in Fig. S5, the ROS contents in algae cells exposed to GO, Cd^{2+}, and GO+Cd^{2+} accounted for 34.2 %, 1.1 − 34.1 %, and 8.8–24.2 % higher than those in the control group, respectively. Ahamed et al. (2020) reported that reduced GO mitigated cadmium-induced oxidative stress and cytotoxicity in HepG2 cells. However, the relative ROS in the GO+Cd^{2+} group (especially at 1 mg/L) were nonmonotonic, not in accordance with the expected toxicity.

The aggregation of highly concentrated GO in the presence of Cd^{2+} (Fig. S3) might contribute to this nonmonotonic response. Similar phenomena have been reported in the algal toxicity of zeolitic imidazolate framework materials (Zhang et al., 2021). In addition to cellular ROS generation, GO with a sharp edge (Fig. 1SA-1E) could contact algal cells, causing physical damage to the cell walls and membranes and potentially increasing algal cell permeability, which was studied and discussed in the SEM and TEM images in the following section.

3.5. Morphological and ultrastructural alterations in algal cells

The morphological alterations of algae exposed to GO, Cd^{2+}, and GO+Cd^{2+} were investigated using SEM (Fig. 3E-H and Fig. S6), and all exposure groups, especially, the GO+Cd^{2+} group, showed severe cell deformation and cell damage (the details were provided in the Supporting Information). Moreover, the ultrastructural alterations of algal cells with GO, Cd^{2+}, and GO+ Cd^{2+} treatment were further illustrated using TEM (Fig. 3I-L). Typical TEM images of control algal cells ($n > 15$) exhibited intact ultrastructural morphology, such as cell walls, cell nuclei, chloroplasts, and other cytoplasmic compartments (Fig. 3I). And the cell walls and cytoplasm were tightly stuck to the plasma membrane (Fig. 3I). Conversely, GO, Cd^{2+} and GO+Cd^{2+} damaged the algal ultrastructure (Fig. 3J-L). The chloroplast and mitochondria damage of GO+Cd^{2+} was more severe than that of GO or Cd based on blurring (Fig. 3J-L), which confirmed the chlorophyll b content (Fig. 3B) and mitochondrial membrane damage (Fig. 3C) results. Moreover, the cell walls exposed to all treatment groups were damaged (marked by the blue arrows). The algal cells underwent significant plasmolysis (marked by green double arrows), which was in accordance with the cell permeability trend (Fig. 3C). Similar phenomena were also observed in GO- and Cd-exposed algae in a previous study (Hu et al., 2014; Zsiros et al., 2020). The quantitative plasmolysis level based on the analysis of the TEM images (Fig. 3M, $n > 15$) was ranked as follows: GO+Cd^{2+} (24.5 %) > Cd^{2+} (20.9 %) > GO (17.1 %). The result demonstrated that GO+Cd^{2+} induced stronger plasmolysis than GO or Cd^{2+} to algal cells, which is consistent with the SEM images. After exposure to GO, Cd^{2+}, and GO+Cd^{2+}, black flake-like particles and/or electron-dense deposits (donated by red circles) were found in vacuoles (Fig. 3J-L). Our previous study confirmed that small GO nanosheets were internalized and located in vacuoles *C. vulgaris* (Ouyang et al., 2020). Thus, we speculate that the above flake-like particles should be GO or GO+Cd^{2+} nanosheets. Subsequently, TEM-EDS mapping was used to further confirm that Cd^{2+} with or without GO nanosheets (Fig. S7). However, there were no noticeable differences in Cd element mapping among the control, GO, and Cd^{2+} treatment groups. Therefore, TEM-EDS mapping failed to track the cell internalization of Cd^{2+} or GO+Cd^{2+}. The above phenomenon may be caused by the instrument detection limit and disturbance of the stain (uranyl acetate). The specific uptake pathways of Cd were discussed below.

3.6. Effects of GO on the cellular uptake of Cd

The cellular uptake of pollutants (e.g., nanoparticles and toxic heavy metals) and their associated pathways have a direct impact on intracellular distribution and cytotoxicity (Cheng et al., 2022; Jiang et al., 2020). Compared with EDS mapping, ICP–MS is a more common and sensitive tool for the quantitatively analyzing toxic heavy metal elements (e.g., Cd) in cells. As shown in Fig. 3N, the ICP–MS results quantitatively showed that the total Cd content related to algal cells was 0.16–0.19, 1.53–1.62, and 66.43–71.98 μg/10^6 cells in the Cd^{2+} treatment (Cd^{2+} and GO+Cd^{2+} groups) at 0.01, 0.1 and 1.0 mg/L, respectively. Therefore, there were significant positive correlations between the accumulation of Cd in *C. vulgaris* and the Cd exposure concentrations. The Cd content of algal cells in the Cd^{2+} exposure groups was significantly ($p < 0.05$) higher than the control and GO groups. The cellular total Cd content measured by ICP–MS was defined as the cell-associated Cd concentration resulting from both intracellular and cell wall-bound Cd. As shown in Fig. 3O, under 1 mg/L Cd^{2+} exposure, the intracellular Cd content (19.66 μg/10^6 cells) of GO+Cd^{2+}-exposed group was significantly ($p < 0.05$) higher than that of Cd^{2+}-exposed group (17.83 μg/10^6 cells). This result was consistent with the plasmolysis result (Fig. 3M) and confirmed the SEM result (Fig. 3G-H) that Cd^{2+} could be attached to algal cell walls. Interestingly, the cell wall-bound Cd contents were significantly ($p < 0.05$) higher than the intracellular Cd contents in both the Cd^{2+} and GO+Cd^{2+} groups at 0.01–1 mg/L exposure (Fig. 3O-P). For example, the cell wall-bound Cd contents (48.60–52.32 μg/10^6 cells) were approximately 2.7-fold higher than the intracellular Cd contents in the 1 mg/L Cd^{2+} and GO+Cd^{2+} groups. Overall, the above data suggested that GO enhanced Cd^{2+} internalization, which was consistent with the algal toxicity results such as chlorophyll synthesis, mitochondrial membrane, and ultrastructural damage. On the contrary, GO could reduce the bioavailability and toxicity of nano-ZnO in mitochondrial depolarization, oxidative stress, and membrane damage (Wu et al., 2019). The edge of GO served as a "nanoblade" and could cause severe mechanical damage to algal cells (Cao et al., 2019; Malina et al., 2019), which could provide additional

'channels' for Cd^{2+} to enter algal cells. Cd^{2+} increased the hydrophobic surface area of GO and might enhance the coating of GO on algae (Sanchez et al., 2012; Zhao et al., 2014), thereby improving the bioavailability of Cd^{2+}. The variation of Cd uptake by algal cells was one of the most important mechanisms for the combined effect of GO and Cd^{2+}, which needed further exploration.

3.7. Transcriptomics analysis explaining persistent toxicity

The volcano plots, Venn diagrams, and KEGG pathway enrichment analysis indicated that the disturbance of *C. vulgaris* expression induced by GO+Cd^{2+} was more severe than that caused by GO or Cd^{2+} alone (Fig. S8 and S9, see specific descriptions for Supporting Information). Moreover, protein−protein interaction (PPI) analysis was performed on DEGs associated with photosynthesis (Fig. 4A). Downregulation of PSI and PSII-encoding, PSII maintenance-encoding, and chlorophyll synthesis-encoding transcripts was more remarkable in the GO+Cd^{2+} group than in the GO or Cd^{2+} group alone. The specific comparisons and discussions of these genes were listed in Table S5. The above alterations in the DEGs may imply that the exposure group, especially GO+Cd^{2+}, affected the photosynthetic process by preventing photoactivation and reducing electron transfer in PSII (Srivastava et al., 2021), as confirmed by the decrease in chlorophyll a and b biosynthesis (Fig. S4 and Fig. 3B).

As shown in Fig. 4B, the DEGs involved in endocytosis showed that the genes related to vacuolar protein sorting, such as SKD1, LIP5, and VPS2.1 (top three in endocytosis PPI network) were only in the GO+Cd^{2+} group significantly upregulated. The aforementioned proteins are pivotal components of the endosomal sorting complex required for transport and play significant roles in the energy-dependent endocytosis of small GO (Ahmed et al., 2019; Norgan et al., 2013). The above results indicated that GO+Cd^{2+} induced overexpression of vacuolar protein-sorting to enhance endocytosis compared with the Cd^{2+} group, resulting in the transport of Cd^{2+} into cells through the GO "carrier" (Fig. 4C). Moreover, Cui et al. (2016) reported that the Ni^{2+} inhibited $P2X_7$ receptors on the cell surface, thereby affecting cell exocytosis of single-walled carbon nanotubes. As shown in Fig. 4C, the significant ($p < 0.05$) downregulation of two ABC transporter-related DEGs (ABCG37 and ABCF4) indicated that GO+Cd^{2+} could inhibit the efflux of Cd^{2+} by cellular ABC transporters. Additionally, GO could inhibit efflux transporters by changing the conformation of transmembrane ABC transporters (Liu et al., 2016). The upregulated genes cation efflux (CE) family only in the GO+Cd^{2+} group showed that GO+Cd^{2+} significantly enhanced the efflux function. The expression of Fe^{2+}/Zn^{2+}-regulated (ZIP) transporters (zrt1, ZIP4) and the nramp family contributing to Cd^{2+} uptake (Lu et al., 2019; Yu et al., 2021), was significantly upregulated in the GO+Cd^{2+} group (Table S5). The above results indicated that algal cells were under high Cd stress resistance under the co-exposure of GO and Cd^{2+}. Chelation and vacuolar compartmentalization are common detoxification mechanisms in response to cadmium stress (Sharma et al., 2016). Herein, the expression of heavy metal ATPase (HMA) transporter DEGs (e.g., Os07g0549700, VATP-P1, and VHA-C) related to vacuolar ion pumps was significantly upregulated in Cd^{2+} treatments, especially in the GO+Cd^{2+} groups. The expression of phytochelatin (PC) synthase and metallothionein (MT) -related DEGs (e.g., GC1 and ftsH) was upregulated in the Cd^{2+} and GO+Cd^{2+} groups (Fig. 4C). These results indicated that the GO+Cd^{2+} group indicated a more intense response to Cd stress than the Cd^{2+} group alone, which may be associated with the promotion of Cd^{2+} uptake by GO.

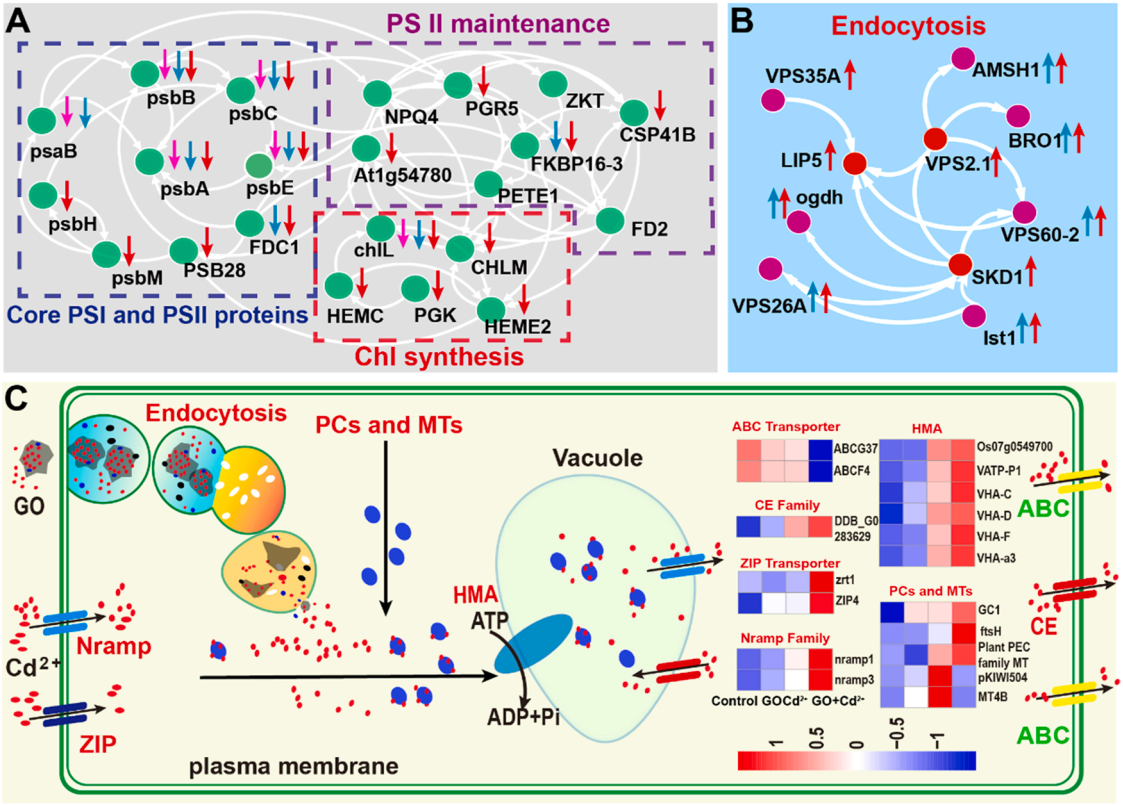

Fig. 4. Transcriptomics analysis of algae exposed to 1 mg/L GO, Cd^{2+}, and GO+Cd^{2+} at 96 h. (A) protein-protein interaction network of 22 representative DEGs related to photosynthesis. (B) Protein–protein interaction network of 10 representative DEGs related to protein processing in endoplasmic reticulum. The DEG alterations labeled with pink, green and red arrows were determined based on comparisons of the 1 mg/L GO, Cd^{2+}, and GO+Cd^{2+} groups with the control. (C) Schematic diagram of the Cd defense response in algae and genes related to the uptake, transport, efflux and detoxification of Cd in algal cells. The details of the DEGs were listed in Table S5 in the Supporting Information.

3.8. Integrating metabolomics with transcriptomics to reveal the mechanism of combined toxicity

Thirty-five metabolites (such as amino acids, fatty acids, carbohydrates, and small acids) were identified by analyzing about 220 peaks using GC–MS. For metabolites, the relative amounts of the metabolites in the treatment and control groups were indicated by heatmap, and the groups were divided into two clusters by using a hierarchical cluster (HCL) analysis: the control/GO/Cd^{2+} and GO+Cd^{2+} exposure clusters (Fig. S10A). Moreover, principal component analysis (PCA) models further confirmed the disparities in the molecular response between the GO+Cd^{2+} exposure group and other exposure groups (Fig. S10B). This result was in accord with the transcriptomics results (Fig. S8). Fig. S10C–E shows that the metabolic pathways associated with amino acids, carbohydrates, and energy metabolism were significantly affected by GO, Cd^{2+}, and GO+Cd^{2+}. The perturbation numbers of metabolic pathways in the Cd^{2+} and GO+Cd^{2+} groups were higher than those in GO, suggesting that Cd^{2+} and GO+Cd^{2+} induce more significant metabolic toxicity in algal cells than GO. Moreover, several metabolites (amino acids, fatty acids, carbohydrates, and alcohols) were analyzed by ANOVA with Tukey's test to explore the significant differences in exposure groups compared with the control, as shown in Fig. S11. All kinds of metabolites were not significant in the GO group ($p > 0.05$). However, compared with the control and GO group, the levels of amino acid metabolites were significantly ($p < 0.05$) decreased in Cd^{2+} and GO+Cd^{2+}-exposed groups. Moreover, compared with the GO treatment groups, and the levels of carbohydrates were significantly ($p < 0.05$) increased in Cd-exposed groups ($p < 0.05$). The above analysis suggested that GO induced different Cd^{2+} metabolic toxicity.

Based on KEGG pathway enrichment analysis, gene and metabolic pathways were combined to further integrate the results of transcriptomics and metabolomics. According to the combined cytotoxicity results (Fig. 3), GO nanosheets augment the phytotoxicity (e.g., chlorophyll b and MMP loss) of Cd^{2+} on *C. vulgaris*. The associations between DEGs and metabolites related to the above-mentioned combined cytotoxicity index were shown in Fig. 5. L-glutamate is a precursor to participating in porphyrin and chlorophyll synthesis (Lu et al., 2019). Here, L-glutamate was significantly decreased by 0.72-, 0.48-, and 0.52-fold in the GO, Cd^{2+}, and GO+Cd^{2+} groups, respectively. The genes related to chlorophyll synthesis precursors (e.g., porphobilinogen

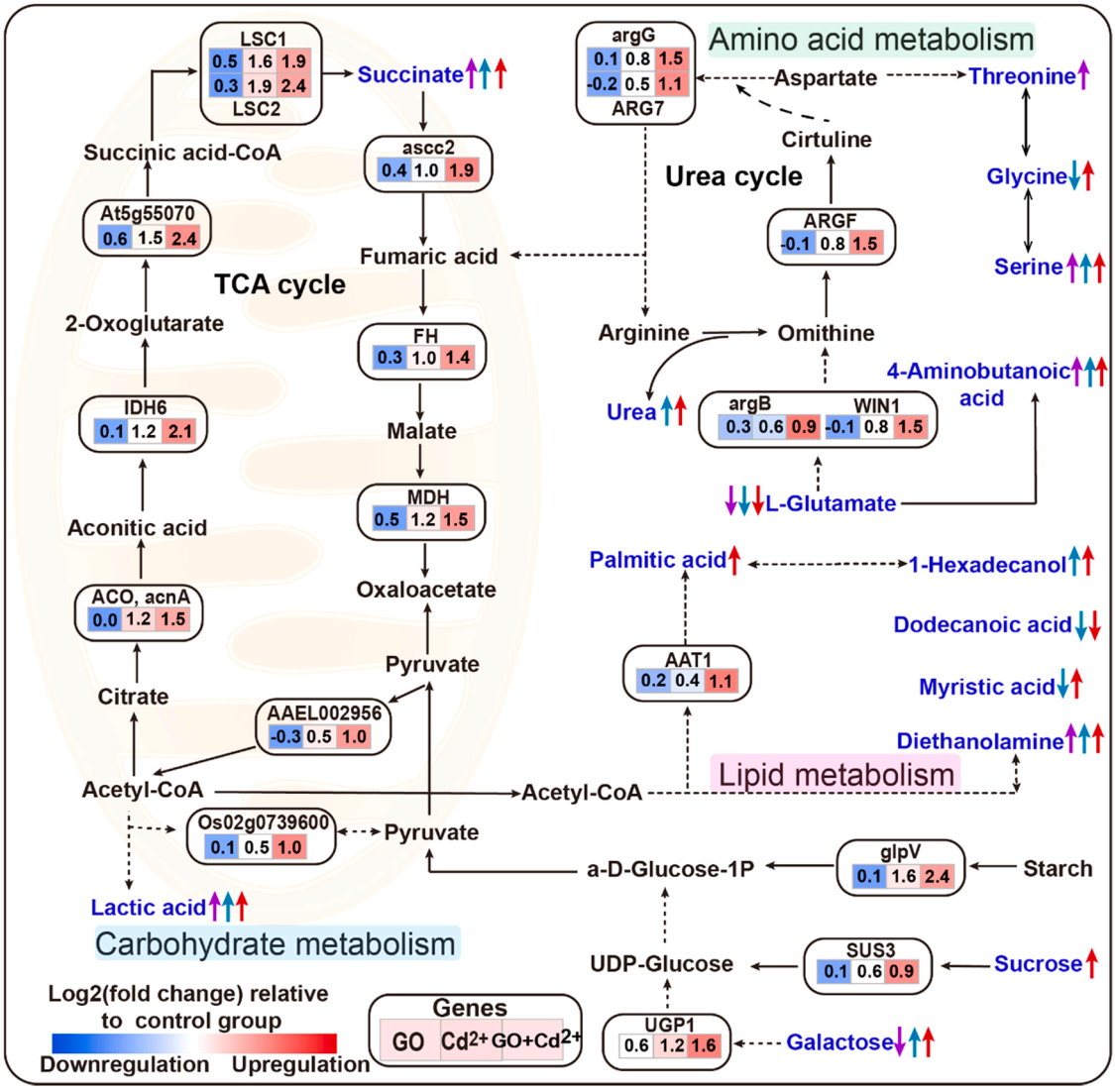

Fig. 5. Connections between the metabolites and DEGs in algal cells. network combining the metabolic pathways and gene alterations in the exposed- groups. The metabolic pathways were constructed based on the Kyoto Encyclopedia of Genes and Genomes (KEGG) pathway database. The blue text denotes metabolites that were detected in the present work. The metabolomics alterations labeled with pink, green and red arrows were determined based on comparisons of the 1 mg/L GO, Cd^{2+}, and GO+Cd^{2+} groups with the control, respectively. The upward-facing arrows and downward-facing arrows indicate metabolites that were upregulated or downregulated compared to the control group, respectively.

synthase genes-HEMB and HEMC, magnesium-protoporphyrin O-methyltransferase gene-CHLM) were significantly downregulated only in the GO+Cd^{2+} group (Table S5). Moreover, fatty acid metabolism was sensitive to physiological health, and palmitic acid was correlated with the chlorophyll content (Tayemeh et al., 2020). Palmitic acid was upregulated (1.41-fold) in the GO+Cd^{2+} group, which was higher than that in GO (1.03-fold) and Cd^{2+} (1.04- fold) groups alone (Table S6). The changes in these metabolomic and transcriptomic data indicated that the GO+Cd^{2+} group caused more severe photosynthetic stress, and GO augmented the algal toxicity of Cd in chlorophyll (especially chlorophyll b) synthesis.

Mitochondria serve as major energy production centers and are generally considered toxicity targets of contaminants (B. Sun et al., 2022; Q. Sun et al., 2022; Zeng et al., 2021). The energy metabolic pathways connected with carbohydrate metabolism, including the tricarboxylic cycle (TCA cycle) and starch and sucrose metabolism, were promoted in all exposed groups compared with the control group, especially in the GO+Cd^{2+} group (Fig. 5, Table S6). For example, sucrose and galactose were upregulated by 1.97- and 4.75-fold in the GO+Cd^{2+} group, respectively, higher than that of in the GO-exposed group (1.11- and 0.83-fold) and Cd^{2+}-exposed group (1.14- and 2.6-fold) (Table S6). The related genes- SUS3 and UGP1, were upregulated in all exposure groups, especially in the GO+Cd^{2+} group (Fig. 5). Fatty acids and amino acids can participate in the TCA cycle through acetyl-CoA (Spinelli and Haigis, 2018). The metabolites related to lipid and amino acid metabolism were upregulated (Fig. 5, Table S6), while associated DEGs were enriched for fatty acid degradation in the GO+Cd^{2+} group (Fig. S9E). The above phenomenon indicated that GO+Cd^{2+} promoted the TCA cycle more deeply than that of the GO and Cd^{2+} exposure alone, that is, the algal cells exposed to GO+Cd^{2+} suffered more serious environmental stress.

Besides the TCA cycle, oxidative phosphorylation can also provide energy efficiency in mitochondria (Kadenbach, 2021). A total of 20 genes related to four complexes composing oxidative phosphorylation were regulated considerably in the exposed groups compared with the control (Table S7). There were 4, 7, and 16 subunits of complexes significantly regulated in the GO, Cd^{2+}, and GO+Cd^{2+} groups, respectively, suggesting more severe damage to the oxidative phosphorylation induced by GO+Cd^{2+} treatment. Both complex II and III are the major ROS generation sites in mitochondria (Nolfi-Donegan et al., 2020). In the GO+Cd^{2+} group, the genes- dhb and CYC1–2, were significantly upregulated by 2.62- and 1.89-fold, respectively, with higher expression than that of the Cd^{2+}-exposed group (2.04- and 1.79- fold) and that of the GO-exposed group (1.22- and 1.23- fold), implying the overproduction of ROS. Subsequently, ROS significantly activated the overexpression of genes related to autophagy-related proteins (e.g., ATG4b and ATG3) (Table S8) only in the GO+Cd^{2+} group, which triggered more serious mitophagy damage and MMP loss (Fang et al., 2021; Yang et al., 2022). The genes related to complex V responsible for synthesizing ATP from ADP were only significantly upregulated in the GO+Cd^{2+} group, indicating increased ATP production in the GO+Cd^{2+} group. The high ATP production might be related to the severe mitochondrial damage caused by GO+Cd^{2+} (Lu et al., 2020). In addition, intracellular Cd^{2+} could enhance mitochondrial membrane permeability and lead to the efflux of H^{+}, which was attributed to MMP loss (Lu et al., 2020). The omics analysis provides a new view for the joint effect between GO and Cd^{2+} on algae in water environments.

4. Conclusions

In this study, Cd^{2+} exhibited a high adsorption capacity (120.56 ± 3.03 mg/g) and strong adsorption affinity (K_L=0.85 ± 0.13 L/mg) for GO. Diverse analytical methods (e.g., UV–vis, EPR, and 2DCOS) were integrated to illustrate the interaction behavior and favorable adsorption sites for Cd^{2+} on GO. The results revealed that Cd^{2+} bonded to the GO nanosheets mainly through cation− π interactions. Cd^{2+} inhibited the colloidal stability of GO in the BG-11 medium. Undoubtedly, combined ecological and health risk assessment of GO and Cd^{2+} at environmental predicted concentration is also worth investigating. Unlike the mitigation effect of humic acid or nanocolloids on the phytotoxicity of GO (Ouyang et al., 2020; J. Zhao et al., 2020), the algal cytotoxicity was obviously enhanced by the combination of GO and Cd^{2+}. Specifically, Cd^{2+} induced more serious biological effects (e.g., growth inhibition and ultrastructural damage) than GO, and GO promoted the uptake of Cd^{2+} by algal cells. Interestingly, the co-exposure with GO greatly amplified the toxicity (e.g., chlorophyll b, mitochondrial membrane damage, and uptake) of Cd^{2+} to *C. vulgaris*. Omics results revealed that the photosynthesis- and uptake-relevant DEGs (e.g., PGR5, CHLM SKD1A, and BCG37), and metabolic pathway (e.g., amino acids and fatty acids metabolism) could contribute to the above-mentioned increased toxicity. These findings highlighted the environmental relevance of coexisting pollutants (e.g., Cd^{2+}) when assessing the environmental risks of ENMs. In the future, the systematic compound ecological effects (synergy, additive or antagonistic effect) and long-term observation of ENMs and coexisting pollutants on various organisms in natural environment (e.g., rivers or lakes) require thoroughly explored.

CRediT authorship contribution statement

Kangying Wu: Data curation and collection, Writing – original draft. **Qixing Zhou:** Supervision, Writing – review & editing. **Yuhao Li:** Investigation. **Xiangang Hu:** Supervision. **Shaohu Ouyang**: Writing – review & editing, Supervision.

Declaration of Competing Interest

The authors declare that they have no known competing financial interests or personal relationships that could have appeared to influence the work reported in this paper.

Data Availability

The data that has been used is confidential.

Acknowledgments

This work was financially supported by the Natural Science Foundation of China (NO. 42107306, U1906222), Fellowship of China Postdoctoral Science Foundation (NO. 2020M680867), the National Key Research and Development Project (NO. 2019YFC1804100), People's Republic of China as a 111 program (NO. T2017002).

Environmental Implications

Given the ubiquitous heavy metal pollution in natural environments and the release of GBNs into aquatic environments, investigating the interactive processes, and behaviors of GBNs and coexisting heavy metal pollutants is critical to understanding the ecological risks of both GBNs and heavy metals. In this study, integrating multiple analytical methods (e.g., 2DCOS, transcriptomic and metabonomic) to investigate the interaction and algal toxicity mechanism of Cd^{2+} and GO, which revealed that Cd^{2+} bonded to the GO nanosheets mainly through cation− π interactions, and the environmental risks of Cd^{2+} augmented by GO and the defense mechanisms of toxicity.

Appendix A. Supporting information

Supplementary data associated with this article can be found in the online version at doi:10.1016/j.jhazmat.2022.130298.

References

Ahamed, M., Akhtar, M.J., Khan, M.A.M., 2020. Reduced graphene oxide mitigates cadmium-induced cytotoxicity and oxidative stress in HepG2 cells. Food Chem. Toxicol. 143, 111515.

Ahmed, I., Akram, Z., Iqbal, H.M.N., Munn, A.L., 2019. The regulation of endosomal sorting complex required for transport and accessory proteins in multivesicular body sorting and enveloped viral budding - an overview. Int. J. Biol. Macromol. 127, 1–11.

Akhavan, O., 2015. Bacteriorhodopsin as a superior substitute for hydrazine in chemical reduction of single-layer graphene oxide sheets. Carbon 81, 158–166.

Akhavan, O., Ghaderi, E., 2010. Toxicity of graphene and graphene oxide nanowalls against bacteria. ACS Nano 4 (10), 5731–5736.

Akhavan, O., Ghaderi, E.J.C., 2012. Escherichia coli bacteria reduce graphene oxide to bactericidal graphene in a self-limiting manner. Carbon 50 (5), 1853–1860.

Akhavan, O., Abdolahad, M., Abdi, Y., Mohajerzadeh, S., 2011. Silver nanoparticles within vertically aligned multi-wall carbon nanotubes with open tips for antibacterial purposes. J. Mater. Chem. 21 (2), 387–393.

Akhavan, O., Ghaderi, E., Emamy, H., Akhavan, F., 2013. Genotoxicity of graphene nanoribbons in human mesenchymal stem cells. Carbon 54, 419–431.

Akhavan, O., Bijanzad, K., Mirsepah, A., 2014. Synthesis of graphene from natural and industrial carbonaceous wastes. RSC Adv. 4 (39), 20441–20448.

Akhavan, O., Ghaderi, E., Hashemi, E., Akbari, E.J.C., 2015. Dose-dependent effects of nanoscale graphene oxide on reproduction capability of mammals. Carbon 95, 309–317.

Akhavan, O., Hashemi, E., Zare, H., Shamsara, M., Taghavinia, N., Heidari, F.J.M.S., C, E., 2016. Influence of heavy nanocrystals on spermatozoa and fertility of mammals. Mater. Sci. Eng. C -Mater. Biol. Appl. 69, 52–59.

Audira, G., Lee, J.S., Siregar, P., Malhotra, N., Rolden, M.J.M., Huang, J.C., Hsiao, C.D., 2021. Comparison of the chronic toxicities of graphene and graphene oxide toward adult zebrafish by using biochemical and phenomic approaches. Environ. Pollut. 278, 116907.

Cao, X., Ma, C., Zhao, J., Musante, C., White, J.C., Wang, Z., Xing, B., 2019. Interaction of graphene oxide with co-existing arsenite and arsenate: Adsorption, transformation and combined toxicity. Environ. Int. 131, 104992.

Chen, L., Shi, G., Shen, J., Peng, B., Zhang, B., Wang, Y., Fang, H., 2017. Ion sieving in graphene oxide membranes via cationic control of interlayer spacing. Nature 550 (7676), 415–418.

Chen, W., Teng, C., Qian, C., Yu, H., 2019. Characterizing properties and environmental behaviors of dissolved organic matter using two-dimensional correlation spectroscopic analysis. Environ. Sci. Technol. 53 (9), 4683–4694.

Cheng, M., Zhou, Q., Wang, L., Jiao, Y., Liu, Y., Li, T., Huang, X., 2022. A new mechanism by which environmental hazardous substances enhance their toxicities to plants. J. Hazard. Mater. 421, 126802.

Cho, K., Cho, D.H., Heo, J., Kim, U., Lee, Y.J., Choi, D.Y., Kim, H.S., 2019. Nitrogen modulation under chemostat cultivation mode induces biomass and lipid production by *Chlorella vulgaris* and reduces antenna pigment accumulation. Bioresour. Technol. 281, 118–125.

Cui, X., Wan, B., Guo, L., Yang, Y., Ren, X., 2016. Insight into the mechanisms of combined toxicity of single-walled carbon nanotubes and nickel ions in Macrophages: role of P2X(7) receptor. Environ. Sci. Technol. 50 (22), 12473–12483.

Ebrahimi, M., Asadi, M., Akhavan, O., 2022. Graphene-based nanomaterials in fighting the most challenging viruses and immunogenic disorders. ACS Biomater. Sci. Eng. 8 (1), 54–81.

Fang, Y., Xing, C., Wang, X., Cao, H., Zhang, C., Guo, X., Yang, F., 2021. Activation of the ROS/HO-1/NQO1 signaling pathway contributes to the copper-induced oxidative stress and autophagy in duck renal tubular epithelial cells. Sci. Total Environ. 757, 143753.

Gao, Y., Ren, X., Wu, J., Hayat, T., Alsaedi, A., Cheng, C., Chen, C., 2018. Graphene oxide interactions with co-existing heavy metal cations: adsorption, colloidal properties and joint toxicity. Environ. Sci. -Nano 5 (2), 362–371.

Goodwin Jr., D.G., Adeleye, A.S., Sung, L., Ho, K.T., Burgess, R.M., Petersen, E.J., 2018. Detection and quantification of graphene-family nanomaterials in the environment. Environ. Sci. Technol. 52 (8), 4491–4513.

Hashemi, E., Akhavan, O., Shamsara, M., Daliri, M., Dashtizad, M., Farmany, A., 2016. Synthesis and cyto-genotoxicity evaluation of graphene on mice spermatogonial stem cells. Colloids Surf. B 146, 770–776.

Hashmi, A., Nayak, V., Singh, K.R., Jain, B., Baid, M., Alexis, F., Singh, A.K., 2022. Potentialities of graphene and its allied derivatives to combat against SARS-CoV-2 infection. Mater. Today Adv. 13, 100208.

Heerema, S.J., Dekker, C., 2016. Graphene nanodevices for DNA sequencing. Nat. Nanotechnol. 11 (2), 127–136.

Hu, X., Lu, K., Mu, L., Kang, J., Zhou, Q., 2014. Interactions between graphene oxide and plant cells: Regulation of cell morphology, uptake, organelle damage, oxidative effects and metabolic disorders. Carbon 80, 665–676.

Hu, X., Kang, W., Mu, L., 2017. Aqueously released graphene oxide embedded in epoxy resin exhibits different characteristics and phytotoxicity of *Chlorella vulgaris* from the pristine form. Environ. Sci. Technol. 51 (10), 5425–5433.

Huh, S.H., 2014. X-ray diffraction of multi-layer graphenes: Instant measurement and determination of the number of layers. Carbon 78, 617–621.

Jannesari, M., Akhavan, O., Madaah Hosseini, H.R., Bakhshi, B., 2020. Graphene/CuO_2 nanoshuttles with controllable release of oxygen nanobubbles promoting interruption of bacterial respiration. ACS Appl. Mater. Interfaces 12 (32), 35813–35825.

Jiang, T., Amadei, C.A., Gou, N., Lin, Y., Lan, J., Vecitis, C.D., Gu, A.Z., 2020. Toxicity of single-walled carbon nanotubes (SWCNTs): effect of lengths, functional groups and electronic structures revealed by a quantitative toxicogenomics assay. Environ. Sci. -Nano 7 (5), 1348–1364.

Kadenbach, B., 2021. Complex IV-The regulatory center of mitochondrial oxidative phosphorylation. Mitochondrion 58, 296–302.

Lavoie, M., Campbell, P.G.C., Fortin, C., 2014. Predicting cadmium accumulation and toxicity in a green alga in the presence of varying essential element concentrations using a biotic ligand model. Environ. Sci. Technol. 48 (2), 1222–1229.

Le Faucheur, S., Behra, R., Sigg, L., 2005. Phytochelatin induction, cadmium accumulation, and algal sensitivity to free cadmium ion in Scenedesmus vacuolatus. Environ. Toxicol. Chem. 24 (7), 1731–1737.

Lee, B.M., Hur, J., 2016. Adsorption behavior of extracellular polymeric substances on graphene materials explored by fluorescence spectroscopy and two-dimensional fourier transform infrared correlation spectroscopy. Environ. Sci. Technol. 50 (14), 7364–7372.

Li, B., Jin, X., Lin, J., Chen, Z., 2018. Green reduction of graphene oxide by sugarcane bagasse extract and its application for the removal of cadmium in aqueous solution. J. Clean. Prod. 189, 128–134.

Li, D., Zhou, Q., Hu, X., Mu, L., Zeng, H., Luo, J., 2022. Environmental decomposition and remodeled phytotoxicity of framework-based nanomaterials. J. Hazard. Mater. 422, 126846.

Liu, S., Jiang, W., Wu, B., Yu, J., Yu, H., Zhang, X., Cherr, G.N., 2016. Low levels of graphene and graphene oxide inhibit cellular xenobiotic defense system mediated by efflux transporters. Nanotoxicology 10 (5), 597–606.

Liu, S., Zeng, T., Hofmann, M., Burcombe, E., Wei, J., Jiang, R., Chen, Y., 2011. Antibacterial activity of graphite, graphite oxide, graphene oxide, and reduced graphene oxide: membrane and oxidative stress. ACS Nano 5 (9), 6971–6980.

Lu, J., Ma, Y., Xing, G., Li, W., Kong, X., Li, J., Yang, J., 2019. Revelation of microalgae's lipid production and resistance mechanism to ultra-high Cd stress by integrated transcriptome and physiochemical analyses. Environ. Pollut. 250, 186–195.

Lu, Z., Wang, S., Ji, C., Li, F., Cong, M., Shan, X., Wu, H., 2020. iTRAQ-based proteomic analysis on the mitochondrial responses in gill tissues of juvenile olive flounder Paralichthys olivaceus exposed to cadmium. Environ. Pollut. 257, 113591.

Malina, T., Marsalkova, E., Hola, K., Tucek, J., Scheibe, M., Zboril, R., Marsalek, B., 2019. Toxicity of graphene oxide against algae and cyanobacteria: nanoblade-morphology-induced mechanical injury and self-protection mechanism. Carbon 155, 386–396.

Noda, I., 2004. Advances in two-dimensional correlation spectroscopy. Vib. Spectrosc. 36 (2), 143–165.

Nolfi-Donegan, D., Braganza, A., Shiva, S., 2020. Mitochondrial electron transport chain: Oxidative phosphorylation, oxidant production, and methods of measurement. Redox Biol. 37, 101674.

Norgan, A.P., Davies, B.A., Azmi, I.F., Schroeder, A.S., Payne, J.A., Lynch, G.M., Katzmann, D.J., 2013. Relief of autoinhibition enhances Vta1 activation of Vps4 via the Vps4 stimulatory element. J. Biol. Chem. 288 (36), 26147–26156.

Obreja, A.C., Cristea, D., Gavrila, R., Schiopu, V., Dinescu, A., Danila, M., Comanescu, F., 2013. Isocyanate functionalized graphene/P3HT based nanocomposites. Appl. Surf. Sci. 276, 458–467.

Ouyang, S., Zhou, Q., Zeng, H., Wang, Y., Hu, X., 2020. Natural nanocolloids mediate the phytotoxicity of graphene oxide. Environ. Sci. Technol. 54 (8), 4865–4875.

Peng, Z., Liu, X., Zhang, W., Zeng, Z., Liu, Z., Zhang, C., Yuan, X., 2020. Advances in the application, toxicity and degradation of carbon nanomaterials in environment: a review. Environ. Int. 134, 105298.

Perreault, F., de Faria, A.F., Elimelech, M., 2015. Environmental applications of graphene-based nanomaterials. Chem. Soc. Rev. 44 (16), 5861–5896.

Ruan, G., Sun, Z., Peng, Z., Tour, J.M., 2011. Growth of graphene from food, insects, and waste. ACS Nano 5 (9), 7601–7607.

Sanchez, V.C., Jachak, A., Hurt, R.H., Kane, A.B., 2012. Biological interactions of graphene-family nanomaterials: an interdisciplinary review. Chem. Res. Toxicol. 25 (1), 15–34.

Scott, D.T., McKnight, D.M., Blunt-Harris, E.L., Kolesar, S.E., Lovley, D.R., 1998. Quinone moieties act as electron acceptors in the reduction of humic substances by humics-reducing microorganisms. Environ. Sci. Technol. 32 (19), 2984–2989.

Sharma, S.S., Dietz, K.J., Mimura, T., 2016. Vacuolar compartmentalization as indispensable component of heavy metal detoxification in plants. Plant, Cell Environ. 39 (5), 1112–1126.

Sivaranjan, K., Padmaraj, O., Santhanalakshmi, J., Sathuvan, M., Sathiyaseelan, A., Sagadevan, S., 2020. Effect of Hybrid mono/bimetallic nanocomposites for an enhancement of catalytic and antimicrobial activities. Sci. Rep. 10 (1), 2586.

Spinelli, J.B., Haigis, M.C., 2018. The multifaceted contributions of mitochondria to cellular metabolism. Nat. Cell Biol. 20 (7), 745–754.

Srivastava, A., Biswas, S., Yadav, S., Kumar, S., Srivastava, V., Mishra, Y., 2021. Acute cadmium toxicity and post-stress recovery: insights into coordinated and integrated response/recovery strategies of Anabaena sp. PCC 7120. J. Hazard. Mater. 411, 124822.

Sun, B., Zhang, Y., Liu, X., Wang, K., Yang, Y., Zhu, L., 2022. Impacts of photoaging on the interactions between graphene oxide and proteins: mechanisms and biological effect. Water Res. 216, 118371.

Sun, Q., Li, Y., Shi, L., Hussain, R., Mehmood, K., Tang, Z., Zhang, H., 2022. Heavy metals induced mitochondrial dysfunction in animals: Molecular mechanism of toxicity. Toxicology 469, 153136.

Tan, P., Sun, J., Hu, Y., Fang, Z., Bi, Q., Chen, Y., Cheng, J., 2015. Adsorption of Cu^{2+}, Cd^{2+} and Ni^{2+} from aqueous single metal solutions on graphene oxide membranes. J. Hazard. Mater. 297, 251–260.

Tayemeh, M.B., Esmailbeigi, M., Shirdel, I., Joo, H.S., Johari, S.A., Banan, A., Tabarrok, M., 2020. Perturbation of fatty acid composition, pigments, and growth indices of Chlorella vulgaris in response to silver ions and nanoparticles: A new

holistic understanding of hidden ecotoxicological aspect of pollutants. Chemosphere 238, 124576.
Vanrompay, H., Skorikov, A., Bladt, E., Beche, A., Freitag, B., Verbeeck, J., Bals, S., 2021. Fast versus conventional HAADF-STEM tomography of nanoparticles: advantages and challenges. Ultramicroscopy 221, 113191.
Wu, B., Wu, J., Liu, S., Shen, Z., Chen, L., Zhang, X., Ren, H., 2019. Combined effects of graphene oxide and zinc oxide nanoparticle on human A549 cells: bioavailability, toxicity and mechanisms. Environ. Sci. -Nano 6 (2), 635–645.
Xie, Q., Liu, N., Lin, D., Qu, R., Zhou, Q., Ge, F., 2020. The complexation with proteins in extracellular polymeric substances alleviates the toxicity of Cd (II) to *Chlorella vulgaris*. Environ. Pollut. 263, 114102.
Xu, L., Xu, M., Wang, R., Yin, Y., Lynch, I., Liu, S., 2020. The Crucial role of environmental coronas in determining the biological effects of engineered nanomaterials. Small 16 (36), 2003691.
Yang, K., Chen, B., Zhu, X., Xing, B., 2016. Aggregation, adsorption, and morphological transformation of graphene oxide in aqueous solutions containing different metal cations. Environ. Sci. Technol. 50 (20), 11066–11075.
Yang, M., Wang, W., 2022. Differential cascading cellular and subcellular toxicity induced by two sizes of nanoplastics. Sci. Total Environ. 829, 154593.
Yao, N., Zhang, X., Yang, Z., Yang, W., Tian, Z., Zhang, L., 2018. Norfloxacin and bisphenol-a removal using temperature-switchable graphene oxide. ACS Appl. Mater. Interfaces 10 (34), 29083–29091.
Yao, N., Li, C., Yu, J., Xu, Q., Wei, S., Tian, Z., Shen, J., 2020. Insight into adsorption of combined antibiotic-heavy metal contaminants on graphene oxide in water. Sep. Purif. Technol. 236, 116278.
Yu, H., Zhen, J., Leng, J., Cai, L., Ji, H., Keller, B., 2021. Zinc as a countermeasure for cadmium toxicity. Acta Pharmacol. Sin. 42 (3), 340–346.
Zeng, H., Hu, X., Zhou, Q., Luo, J., Hou, X., 2022. Extracellular polymeric substances mediate defect generation and phytotoxicity of single-layer MoS_2. J. Hazard. Mater. 429, 128361.
Zeng, W., Yu, Q., Wang, D., Liu, J., Yang, Q., Zhou, Z., Zeng, Y., 2021. Mitochondria-targeting graphene oxide nanocomposites for fluorescence imaging-guided synergistic phototherapy of drug-resistant osteosarcoma. J. Nanobiotechnol. 19 (1), 79.
Zhang, X., Shen, J., Zhuo, N., Tian, Z., Xu, P., Yang, Z., Yang, W., 2016. Interactions between antibiotics and graphene-based materials in water: a comparative experimental and theoretical investigation. ACS Appl. Mater. Interfaces 8 (36), 24273–24280.
Zhang, X., Hu, X., Wu, H., Mu, L., 2021. Persistence and recovery of ZIF-8 and ZIF-67 phytotoxicity. Environ. Sci. Technol. 55 (22), 15301–15312.
Zhao, J., Wang, Z.Y., White, J.C., Xing, B., 2014. Graphene in the aquatic environment: adsorption, dispersion, toxicity and transformation. Environ. Sci. Technol. 48 (17), 9995–10009.
Zhao, J., Ning, F., Cao, X., Yao, H., Wang, Z., Xing, B., 2020. Photo-transformation of graphene oxide in the presence of co-existing metal ions regulated its toxicity to freshwater algae. Water Res. 176, 115735.
Zhao, Y., Liu, Zhang, X., Liao, W., 2021. Environmental transformation of graphene oxide in the aquatic environment. Chemosphere 262, 127885.
Zhu, X., Hu, Y., Wu, G., Chen, W., Bao, N.Z., 2021. Two-dimensional nanosheets-based soft electro-chemo-mechanical actuators: recent advances in design, construction, and applications. ACS Nano 15 (6), 9273–9298.
Zsiros, O., Nagy, G., Patai, R., Solymosi, K., Gasser, U., Polgar, T.F., Horcsik, Z.T., 2020. Similarities and differences in the effects of toxic concentrations of cadmium and chromium on the structure and functions of thylakoid membranes in *Chlorella variabilis*. Front. Plant Sci. 11, 1006.